Correlating catalyst ink design and catalyst layer fabrication with electrochemical CO_2 reduction performance

Guangxin Liu [1,2], David McLaughlin[1,2], Simon Thiele[1,2], Chuyen Van Pham [1,*]

1. Forschungszentrum Jülich GmbH, Helmholtz Institute Erlangen-Nürnberg for Renewable Energy (IEK-11), Cauerstr. 1, 91058 Erlangen, Germany
2. Department of Chemical and Biological Engineering, Friedrich-Alexander-Universität Erlangen-Nürnberg, Egerlandstr. 3, 91058 Erlangen, Germany

* Corresponding author: Chuyen Van Pham, c.pham@fz-juelich.de

Abstract: The controllable fabrication of catalyst layers (CL) by tuning the multiscale structure formation is complex but vital to achieving optimum carbon dioxide reduction (CO_2R) performance. An in-depth understanding on the role of each catalyst ink component and how multi-component interactions affect ink status, catalyst layer structure, and CO_2R performance is crucial. In this work, the roles of different ingredients of catalyst ink were systematically investigated from simple binary inks to complete catalyst inks. Silver (Ag) particles-Nafion interactions were found to play a decisive role in stabilizing catalyst ink, mitigating agglomeration and particle sintering. The catalyst ink was comprehensively characterized and reported by static multiple light scattering (SMLS) for the first time in this paper. The evolution of catalyst ink was identified in three stages: stable, flocculation and sedimentation. Isopropanol (IPA)-rich solvents were found to be more effective in stabilizing catalyst ink due to better dispersed Nafion aggregates and further enhanced Ag particle-Nafion interactions. Subsequently, catalyst layer structure and CO_2R performance were correlated with multi-component interactions in catalyst ink. Strong Ag particle-Nafion interactions were proven to promote not only ink stability, but also catalyst layer homogeneity and reaction site distribution. The carbon monoxide (CO) selectivity was boosted from 80.5% to 94% at an industrial meaningful current density of 200 mA/cm^2 using commercial Ag nanoparticles by rational design of ink formulation, dispersing and fabrication processes. Simultaneously, a scalable manufacturing methodology of robust gas diffusion electrodes (GDEs) to achieve optimal CO_2R performance was developed and validated.

Keywords: CO_2 reduction, gas diffusion electrode, catalyst ink, static multiple light scattering, catalyst layer fabrication.

1. Introduction

The increase in atmospheric CO_2 concentration over the past century, primarily caused by anthropogenic carbon dioxide (CO_2) emission from fossil fuels consumption, is considered an essential contributor to climate change [1, 2]. Shifting from fossil fuels to renewable energy has become a widespread consensus. As the low-carbon roadmaps launch and the share of renewable energy in the electricity supply keeps rising in various countries, industrial demand for efficient energy conversion technologies, such as electrochemical CO_2 reduction, is poised to increase. Combined with carbon capture techniques, using renewable energy to electrocatalytically convert CO_2 to fuels and commodity chemicals, like carbon monoxide (CO), ethylene (C_2H_4), alcohols, etc., is a crucial approach to achieving net-zero carbon emission

(Fig. 1) [3]. Among the various products of CO_2 reduction (CO_2R), CO is one of the most valuable due to its wide application as a feedstock in different downstream industrial processes, such as hydrocarbons production by Fischer-Tropsch process, metal smelting and chemicals synthesis [4, 5]. Silver (Ag) has been reported to exhibit high selectivity to CO in H-cells, it is believed to be the most promising catalyst for large-scale industrial applications [3].

The key component of a CO_2R electrolyzer is the gas diffusion electrode (GDE). It typically consists of a gas diffusion layer (GDL, carbon fiber substrate (CFS) coated with a microporous layer (MPL)) and a catalyst layer (CL). The GDL is usually porous, electrically conductive, and hydrophobic. It provides distribution channels for reactants/products and mechanical support for the CL. The catalyst layer, connecting electrolyte (or membrane), active catalyst sites and CO_2, is where CO_2 reduction reactions occur [6]. It is usually a porous structure composed of catalyst nanoparticles and ionomer. An efficient catalyst layer should feature a high electrochemically active area, good electron and ion (H^+ or OH^-) conductivity, enough diffusion channels for reactants/products, and sufficient chemical/mechanical stability [7]. The structures of the CL from micro to macro scale play a crucial role in the performance of a GDE.

The controllable fabrication of CLs by tuning the multiscale structure formation is a complex but vital step for GDE performance optimization. Currently, the most common fabrication method is coating catalyst dispersion, *i.e.,* catalyst ink, on a substrate, such as a GDL or membrane. As illustrated in Fig. 1, the CL fabrication process mainly includes three steps: ink preparation, coating and drying. Generally, catalyst ink is prepared by mixing and dispersing catalyst powder and ionomer in solvents. Due to the high surface energy of nanoparticles, the as-received catalyst powder contains a large amount of agglomerates. The goal of dispersing is to obtain a stable and homogeneous ink by breaking down catalyst agglomerates and boosting interactions between catalyst nanoparticles, ionomer and solvents. Ultrasonication is the most used dispersing technique because of its low cost and easy operation [8]. A recent study on Pt/C ink revealed that longer ultrasonication led to more primary aggregates and fewer large agglomerates. However, long ultrasonication time weakened the adsorption of Nafion on Pt/C particles, resulting in worse performance [9]. Even though ultrasonication has been a benchmark technique for catalyst ink dispersion, its effectiveness for the catalyst ink of CO_2 reduction has yet to be evaluated.

The commonly used ink coating techniques in labs include drop casting, hand painting, inkjet printing, air brushing, ultrasonic spray coating, doctor blading, etc. The ink preparation, GDE manufacturing and performance information for CO_2 reduction in recent publications were summarized in Table S1. Most of the inks were prepared by dispersing catalyst nanoparticles in isopropanol (IPA)/water mixture by ultrasonication with a low solid concentration and coated by air brushing or ultrasonic spray coating. As a manual method, air brushing (also drop casting and hand painting) intrinsically brings great challenges to homogeneous and reproducible CL fabrication. It highly relies on the personal skills of the operator [10]. Ultrasonic spray coating is known for its superior CL homogeneity and catalyst loading controllability [11]. However, the realization of these advantages depends on the precise control of ultra-low flow rate (usually < 1 mL/min) of low solid content ink (usually <3%) [12]. This makes spray coating a slow process, which requires better ink stability. Therefore, for the cases of less stable ink or high catalyst loading, spray coating can only provide in-plane uniformity, but creates gradients of catalyst and ionomer at the through-plane direction of CL (Fig. S1). In fact, the widely used bare metal or metal oxide catalysts for CO_2 reduction usually have a relatively large primary particle size (tens of nm to tens of μm) and the corresponding catalyst inks usually settle quite fast [13, 14]. Insufficient ink stability and inhomogeneous catalyst layer are common problems plaguing the CO_2R research community. They hindered reproducing the good

performance of new catalysts from H-cell to GDE cell. Doctor blading is a suitable technique for high solid content and high-viscosity ink, which provides more efficient fabrication of high catalyst loading and large electrodes. The catalyst loading is controlled by the gap between the blade and substrate. The requirement for ink stability is comparatively lower due to the fast coating process [7]. Therefore, in this work, the application of doctor blading using high-concentration Ag inks is explored with the aim of achieving uniform, fast and reproducible CL manufacturing.

The porous structure of CL forms in the drying stage. The structure evolution in such a multiphase, multi spatial-scale and time-scale process remains unclear. However, CL formation is highly affected by solvents properties (like vapor pressure) and drying conditions (like temperature, humidity, pressure, gas flow rate, etc.), which creates new and continuously changing environments for catalyst particles and ionomer [15–20].

In summary, the influencing factors on CL formation can be grouped into three categories: (i) characteristic parameters of coating techniques, *e.g.,* shear rate, ink flow rate, ultrasonic power, etc., (ii) drying conditions (*vide ante*) and (iii) catalyst ink status (*vide infra*). The influence of ink status on CL formation is exerted not only by the internal interactions of catalyst/solvents, ionomer/solvents and catalyst/ionomer, but also by modulating ink coatability and drying behaviors deeply through ink macro properties, such as stability, viscosity, vapor pressure, etc. [15, 16, 21–23]. Undoubtedly, the ink status plays a decisive role throughout the whole fabrication process of CL.

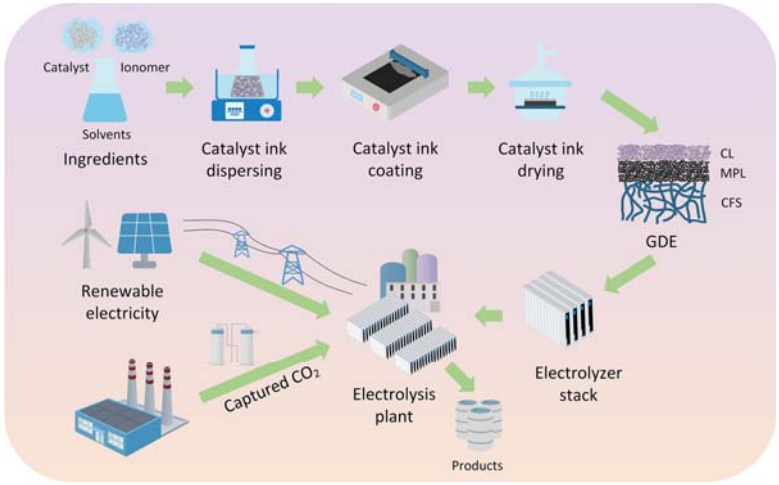

Fig. 1 Illustration of catalyst layer fabrication procedure and electrochemical CO_2 reduction-utilization industry chain.

The catalyst ink status is determined by the inherent properties of each ingredient (*e.g.,* catalyst materials, the molecular structure of ionomer, the physicochemical properties of solvents, etc.), ingredient ratios and dispersing methodology. The characterization of catalyst ink is divided into two categories: microstructure characterization and macro properties characterization. Microstructure characterization includes particle size measurement with dynamic light scattering (DLS), (ultra) small-angle X-ray/neutron scattering ((U)SAXS/SANS), cryo-TEM/SEM, and so on [24–26]. Macro properties of catalyst ink include viscosity, thixotropy, surface tension, ink stability, etc. [21, 27, 28]. Viscosity is a helpful indicator of the strength of ink microstructure and interactions between components. Ink stability is commonly investigated by visual observation and by measuring ζ-potential to indicate the repulsion between particles [21, 25, 29, 30]. Visual observation is a qualitative and insensitive approach, the results can only be reported subjectively as “yes/no” or “more/less” than the reference status after obvious sedimentation

has happened. It can only provide a general impression of ink stability [21, 30]. A wealth of details occurring before visible phase separation are missed, thus the results are usually not helpful for ink coatability evaluation.

In addition, most of the characterization methodologies mentioned above, whether microscale or macroscale approaches, can only provide transient information on ink status. The multi-component interactions and particle behavior evolution with time are more important for ink coating and CL formation, but it was neglected by most researchers. In this work, the sedimentation dynamics and stability of inks with different formulations were characterized using static multiple light scattering (SMLS). According to Mie theory and Beer-Lambert law, the photon mean free path is determined by particle size and volume. The photon mean free path in turn determines the backscattering and transmission light intensity (Fig. S2). Therefore, the collective behaviors of particles, like flocculation, coalescence, sedimentation, creaming, phase separation, etc., can be investigated by detecting the transmission and backscattering light intensity evolution. To our knowledge, this is the first systemic study on the temporal and spatial particle dynamics in catalyst ink.

The objective of this work is to correlate catalyst ink design and catalyst layer fabrication with CO_2R performance. The role of each catalyst ink component, *i.e.,* Ag particles, Nafion, solvents (IPA, EtOH, water), and underlying interactions between them (Ag particles/solvents, Nafion/solvents and Ag particles/Nafion) were decoupled and systematically studied from simple binary inks to complete inks. The sedimentation dynamics of complete inks were characterized by static multiple light scattering with respect to the effect of dispersion techniques, Nafion content, IPA/water ratio and solid content. Subsequently, how these interactions between components affect ink sedimentation, catalyst layer structure and further CO_2R reduction performance was investigated.

2. Experiments and methods

Material and catalyst ink preparation. Catalyst inks were prepared by dispersing commercial Ag nanoparticles (IoLiTec, 50-60 nm, 99.9%) with/without Nafion dispersion (Chemours, D2020) in different alcohols (isopropanol or ethanol, Sigma Aldrich, AR)/water (MilliporeSigma, Mili-Q® IQ 7000, 18.2 MΩ·cm) mixtures. The inks were dispersed by either ultrasonic bath (UB) (VWR, USC-THD) or roller mixing (RM) (Ratek, BTR5). The ultrasonic bath temperature was kept below 30°C with ice during dispersing. The speed of the roller mixer was 180 rpm and 15 g of zirconium dioxide (ZrO_2) grinding balls (Fritsch, 5mm) were used to enhance dispersion. The effects of alcohols, dispersing methods, Nafion content, IPA/water ratio and total solid content were investigated. The ink formulations used in this paper are listed below in Table 1.

Table 1 Ink formulations and preparation

Nafion (wt. %)	Total solid (wt. %)	Alcohol/H_2O (wt. %)	Total weight (mg)	Dispersing method
0	16	0/100, 50/50, 100/0	1000	Ultrasonic bath
20	20	66.7/33.3	6000	Ultrasonic bath
5, 10, 20, 30, 40	20	66.7/33.3	6000	Roller mixing
20	20	0/100, 10/90, 30/70, 50/50, 66.7/33.3, 80/20, 100/0	6000	Roller mixing
20	10, 20, 30, 40	66.7/33.3	6000	Roller mixing

Agglomerate size and ζ-potential measurements. The average agglomerate size and ζ-potential were determined by a dual-angle dynamic light scattering (DLS, 13° and 173°) and electrophoretic light scattering (ELS) apparatus (Malvern Panalytical, Zetasizer Nano ZSP). A helium-neon laser beam (λ=632.8 nm) served as the light source. The samples with a solid content of ~0.015 wt.% were prepared by diluting the original inks 1200 times using corresponding solvents. Three measurements were conducted for each sample and three samples were analyzed for each ink formulation at 20 °C. Stokes-Einstein and Helmholtz-Smoluchowski equations were used to calculate the agglomerate size and ζ-potential respectively. The values of refractive index, viscosity and dielectric constant for dispersion media used in this paper were obtained by fitting the experimental data from literature (Fig. S4).

Ink sedimentation dynamics and stability measurements. The sedimentation dynamics and stability of inks were investigated using static multiple light scattering (SMLS) with Turbiscan Tower (Formulaction) at room temperature. The device equipped an LED as a light source emitting near infrared radiation at a wavelength of 880 nm. Two synchronous detectors were placed at 0° and 135° directions from incident light to record the transmission and backscattering light flux. Any subtle destabilization phenomenon happening in the inks will impact the backscattering and/or transmission signal intensities. Compared with visual observation, SMLS provides much higher sensitivity and quantitative information. 3.6 mL of catalyst ink was extracted into a glass vial, then the sample was scanned every 30 s from bottom to top with a displacement interval of 20 µm. To compare the overall ink destabilization kinetics, a dimensionless instability index (*I*) was defined as the sum of the average intensity variation of transmission or backscattering over the total sample height between two scans. Since all the inks were opaque, only backscattering signals were analyzed. The instability index was calculated according to Eq. 1.

$$I_t = \frac{\sum_0^H |BSI_t(h) - BSI_{t-1}(h)|}{H} + I_{t-1} \quad (1)$$

where H is the total sample height, *t* is the scanning times. *BSI* (*h*) is the backscattering light intensity at the height *h*.

Thermogravimetric analysis (TGA). The catalyst loading was determined by TGA (Setaram, SETSYS Evolution). TGA was conducted under air atmosphere (200 mL/min) with a heating rate of 20 °C/min from 25 °C to 700 °C. The temperature was then held at 700 °C for 15 min to burn out polymers and carbon. The final weight was recorded at 25 °C after cooling down.

GDE fabrication. Catalyst inks were coated on pre-cut GDLs (Freudenberg, H23C2, 16.56 cm^2) with a doctor blade (ZAA 2300, Zehnter). The gap height was set to 300 µm for doctor blading, which resulted in an average catalyst loading of ~2 mg/cm^2. The coated ink was dried at room temperature (22 °C) in a fume hood.

Electrochemical CO_2 reduction performance testing. A three-compartments flow-cell (ElectroCell) was used to conduct electrochemical CO_2 reduction experiments. The doctor-bladed cathode GDE was installed between CO_2 and the catholyte compartment. The anode was a titanium plate coated with Ir-MMO (iridium-mixed metal oxide). Both cathode and anode have an active geometry area of 10 cm^2. A Nafion NR-211 membrane was used to transfer ions and separate catholyte and anolyte compartments. Both catholyte and anolyte were 1 M $KHCO_3$ (Sigma Aldrich, 99.7%) solutions and circulated separately with a peristaltic pump (MasterFlex L/S) at a flow rate of 30 mL/min. The CO_2 (Air Liquide, 99.9995%) flow rate was controlled at 100 mL/min for all experiments by a mass flow controller (Bronkhorst, EL-FLOW® Prestige). To measure and control cathode potential, fitting a reference electrode (RE) to the electrolyte

inlet/outlet is widely adopted. However, the accuracy and reliability of such a configuration are suspicious due to the long distance of WE|RE, the turbulence of electrolyte, and gas bubbles. Instead, a tiny leak-free Ag/AgCl reference electrode (Innovative Instruments, Inc.) with a diameter of 1.6 mm was directly introduced to the catholyte compartment to improve measurement accuracy. The flow-cell configuration and testing setup schematics are illustrated in Fig. S3. All the electrochemical experiments were repeated three times to ensure reproducibility. Polarization curves were obtained by stepwise chronopotentiometry followed by electrochemical impedance spectroscopy (EIS, 0.1-100k Hz) at each current step with a potentiostat (BioLogic, VMP-300). The pH of the catholyte was monitored by an online pH meter (Mettler Toledo, SevenExcellence). The measured potential vs. Ag/AgCl RE was 90% iR-drop compensated and converted to values versus reversible hydrogen electrode (RHE) with equation (Eq. 2). After the stepwise polarization was finished, a constant current of 200 mA/cm^2 was applied for 1 h. CO_2 reduction products were analyzed by an online gas chromatograph (GC, Thermo Scientific, Trace 1310) equipped with an MS5A column, two HayeSep Q columns and two thermal conductivity detectors (TCD). The product composition was measured continuously by the GC for at least three times. The average Faradaic efficiency of each component in 1h was calculated according to Eq. 3.

$$E_{RHE} = E_{\mathrm{Ag/AgCl}} + 0.205 + 0.0591 * pH \quad (2)$$

$$FE = \frac{en\mathrm{F}}{It} \quad (3)$$

where *e* is the number of electrons transferred, *n* is the amount of product in moles, F is the Faraday constant, *I* is total current, *t* is the electrolysis time.

Scanning electron microscopy (SEM). The samples for agglomerates characterization were prepared by drop-casting the dispersions made by diluting the original inks 100 times with corresponding solvents on silicon wafers. The SEM images were acquired with TESCAN Vega 3. The GDE samples were sputter-coated with gold for 20 s. The surface and cross-section morphology was characterized using Zeiss Crossbeam 540 FIB-SEM. To shield the cross-section from unintended beam damage, a platinum protective pad was deposited. However, platinum has poor contrast to silver, hence a thin layer of carbon was electron beam deposited first. This deposition step used a current of 8 nA at an accelerating voltage of 2 kV. Subsequently, the platinum was ion beam deposited using a current of 300 pA, accelerated at 30 kV. With the protective layer in place, the cross-section was excavated by ion milling. The front face was milled by applying a beam current of 7 nA. Last, the front was polished with a current of 700 pA.

Rheology measurements. Rheology measurements were performed with a rheometer (Brookfield, DVNext). Prior to each measurement, the sample was preconditioned at 500 s^{-1} for 40 s. The stepwise steady-shear measurement lasted 30 s for each shear rate and the viscosity data were acquired by averaging 3 points in the last 15 s.

3. Results and discussion

3.1 Interactions of Ag nanoparticles with solvents

It is well known that there are complex self-associations and inter-molecular associations by hydrogen bonds in a wide range of solvents and their mixtures [31–33]. The interactions at the molecular scale have a complicated influence not only on the bulk characteristics of solvents (*e.g.,* viscosity, dielectric constant,

etc. Fig. S4), but also on nanoparticle aggregation in these solvents [34, 35]. As shown in Fig. 2 (a), Ag nanoparticles had the lowest ζ-potential of around -40 mV in pure water, whereas had the highest ζ-potential of around -30 mV in pure alcohols, even though there was a small difference of about 2 mV for those in IPA and EtOH. The higher negative charge density on Ag nanoparticles' surface in water is due to stronger disassociation of water than alcohols. Interestingly, ζ-potential did not respond to the alcohol fraction linearly. The ζ-potentials in 50 wt.% alcohol/water mixtures were almost the same as that in corresponding pure alcohols. We attribute this to the complexation of hydroxyl groups with alcohol molecules [36]. The average agglomerates size of Ag in water decreased from above 2200 nm to below 500 nm after ultrasonication for 30 min. However, the average size evolution in both alcohols featured a V shape. After 2 min of ultrasonication, a minimum in the average size of ~850 nm and ~1400 nm was obtained in IPA and EtOH, respectively. Then after 30 min, the average size returned to the same level as before ultrasonication (Fig. 2 (b)).

Ultrasound as an external energy input was used to disperse Ag nanoparticles. When the ultrasonic waves propagate through the dispersing media, transient cavitation happens. Continuous microbubble collapse has exceedingly high energy density generating turbulent flow and intense shock waves. This induces high-speed collisions among nanoparticles suspending in the dispersing media. It is the violent collision that breaks the agglomerates down. However, an extremely high temperature and pressure (*ca*. 5000 K and 2000 atm) are also generated locally in this process, which can lead to local melting and particle fusion [37–39]. This likely results in the particle size growth in alcohols. Indeed, dense Ag aggregates with different sizes were observed in all three solvents after ultrasonication for 60 min, but large aggregates (>10 μm) in water were much less than that in alcohols (Fig. S5). This indicates Ag nanoparticles are more sensitive to external energy in alcohols. It is probably due to lower |ζ-potential| and higher solubility of the capping agent (fatty acid in this case) in alcohols, which results in weaker repulsive forces between particles [40].

It is noteworthy that although the smallest average particle size was observed in water by DLS, particle coagulation forming clusters was observed after drying (Fig. 3). It was attributed to high capillary force and surface energy in the drying process [35]. This could result in stress concentration, which is one of the most important reasons for the formation of cracks in the catalyst layer. Taken together, Ag agglomerates can be broken down to smaller sizes more efficiently in water, but large clusters form during drying. The particle sintering is more severe in alcohols, but the dispersion in alcohols and CL after drying is more homogeneous (Video S1 and S2, Fig. 3). It is difficult to redisperse Ag agglomerates to primary particles (50-60 nm in this case) since ultrasound induced particle sintering happens simultaneously with agglomerates breaking down.

Further experiments were conducted in alcohol/water mixtures. Opposite trends were observed for IPA/water and EtOH/water mixtures. IPA/water mixture resulted in a neutralizing effect, *i.e.,* most average size values fell between those in single solvents. However, EtOH/water mixture exhibited a superposition effect, the average size increased dramatically than those in single solvents. We ascribe the discrepancy to the different molecule associations and hydrogen-bond networks in the alcohol/water mixtures [33, 41], which further led to different coordination and adsorption characteristics of solvent molecules with Ag nanoparticles [42, 43]. Van der Waals force between particles has been proven to be highly affected by solvent structure and adsorption [44, 45]. Therefore, the Van der Waals attraction between Ag particles in EtOH/water mixture could be much higher than those in other solvents. Considering the bigger

agglomerates sizes in both pure and aqueous EtOH, IPA is a more efficient alcohol for dispersing Ag nanoparticles.

Compared with the weak Brownian movement and fast sedimentation in single solvents, much more intense particle motion and adsorption were observed in both alcohol/water mixtures during drying (Video S3 and S4). The thermal and concentration gradients caused by faster alcohol evaporation led to circulating flows driven by surface tension gradients, pulling catalyst particles to the edge of the ink drop and forming large clusters (Fig. S6) [46]. In addition, our observation showed that phase separation happened in 1 min for all the catalyst inks. It indicated that no stable ink can be achieved only by the interactions between Ag nanoparticles and solvents. The relatively large agglomerates, fast sedimentation, and edge accumulation of catalyst are adverse to coating homogeneity and electrochemically active area. Steric hindrance by adding ionomer in the ink formula is necessary to minimize these phenomena and stabilize catalyst ink (Fig. S7, S8 and Video S5, S6).

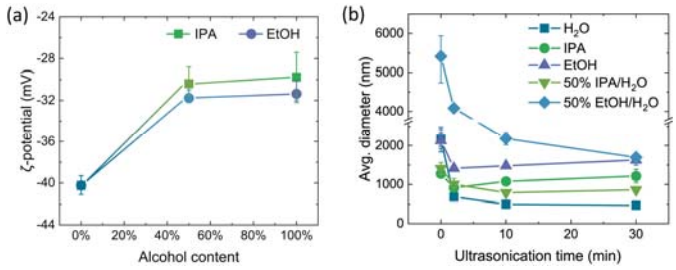

Fig. 2 (a) ζ-potential and (b) average agglomerate size of Ag particles in water, IPA, EtOH and their mixtures.

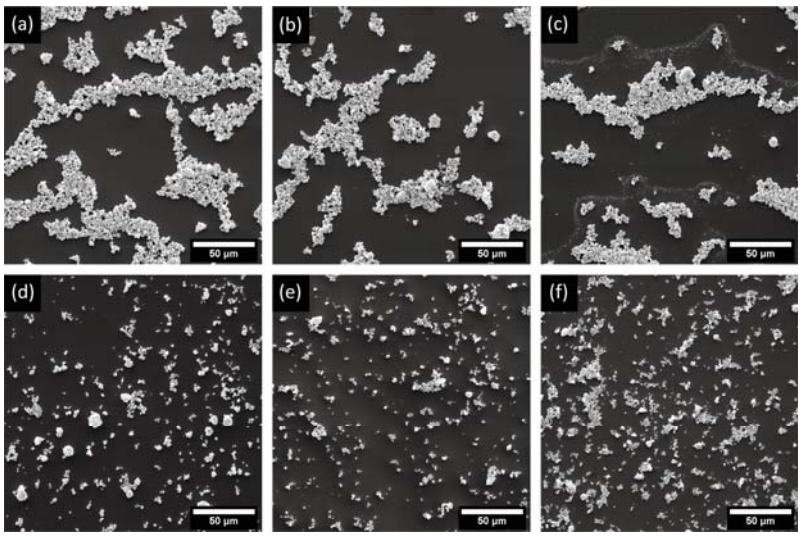

Fig. 3 Ag agglomerates dispersed in water (a, b, c) and IPA (d, e, f) after ultrasonication treatment of 0, 2, 30 min (from left to right).

3.2 Interactions of Nafion with solvents

Before we discuss the complete inks, we will briefly discuss the literature to explore the micro-interactions of Nafion with solvents, which is supposed to bring forward a deeper understanding of the role of Nafion in complete catalyst inks and CO_2 reduction performance. Nafion is comprised of a hydrophobic

polytetrafluoro-ethylene (PTFE) backbone and hydrophilic sulfonated vinyl ether side chains. It is this unique molecular composition that gives Nafion superior proton transport and mechanical functionalities, which enables its wide electrochemical applications, including CO_2 reduction in an acidic or a near-neutral environment [47, 48]. Generally, the proton conductivity of Nafion is dependent on the bonding of SO_3^- groups with H_3O^+ and the following water network, and the hydrophobic backbone matrix controls the mechanical properties[49]. The interesting but complex interactions and balances between backbones, side chains and solvents govern the morphology of Nafion in dispersing media and hydrated film, and further the morphology has a profound influence on the final properties of Nafion in catalyst layer or membrane.

It has been well accepted that Nafion in dispersing media does not form true solutions but suspensions with anisotropic colloidal aggregates. Early studies have revealed a rod-like structure of Nafion aggregates in a series of polar and non-polar solvents (*e.g.*, water, ethanol, formamide, DMF, etc.) with the help of small-angle X-ray/neutron scattering techniques (SAXS/SANS) [50–54]. The rod-like aggregates feature a PTFE backbone core and side chains on the outer surface, they had a radius of around 2-2.5 nm and a length of above 100 nm. The balance of elastic energy (rigidity of PTFE backbone and side chains) and interfacial energy was claimed to control the radii of aggregates.

Recent atomistic molecular dynamics simulation studies tried to correlate Nafion morphology with the polarity of solvents [55, 56]. They found that loose, swollen and more solvated aggregates are formed in low polarity solvents (*e.g.*, toluene, IPA, EtOH, etc.), which was attributed to the higher solubility of the backbone with these solvents and ion-pair clusters on side chains. Experimental studies showed that the SANS and SAXS curves of Nafion in alcohols can be fitted with both a spherical and cylindrical model, and the spherical fitting was even better [57, 58]. Their results revealed that Nafion forms loose, polydisperse, roughly spherical aggregates populations in alcohols with an average diameter of 15.5-17 nm. In contrast, tight and elongated aggregates were observed in high-polarity solvents (*e.g.,* water and formamide). Since the side chains were fully dissociated, the aggregates were mainly controlled by the hydrophobic effect. It is worth noting that only Nafion in water, rather than in all the solvents as reported in early studies, was recognized as elongated rod-like aggregates [55].

As the most common solvents for catalyst ink, alcohol/water mixture strongly affect Nafion morphology by their ratios. With the increase of alcohol/water ratio to around 1:1, the dense cylindrical aggregates in pure water transform into looser and more dispersed swollen clusters (>200 nm) [55, 57–59], but the primary aggregates become smaller in these clusters [59]. Then the particles gradually become the above-mentioned roughly spherical polydisperse populations in pure alcohol. The morphology evolution was also proven by transmission electron micrographs [60, 61]. In brief, Nafion aggregates transformed from very weakly solvated in pure water to more solvated with the addition of alcohol, and less solvated in pure alcohol. The addition of alcohol weakens hydrophobic interactions but enhances electrostatic interactions of Nafion with solvents, which resulted in the morphology evolution of Nafion aggregates.

3.3 Interactions of components in complete catalyst inks

Dispersing techniques. Even though ultrasonic bath is commonly used, serious Ag particle sintering was observed (Section 3.1). Compared with ultrasonication, roller mixing is a milder technique that provides

better consistency and reproducibility. Complete inks with Nafion were dispersed respectively by ultrasonication bath (UB-ink) and roller mixing (RM-ink).

The sedimentation dynamics spectra along ink height (from bottom to top) are shown in Fig. 4(a), (d), Fig. S9(a) and S10(a). The backscattering spectra of inks with different ultrasonication time had in common the feature of decreasing parallel profiles in the first 5 min (Fig. 4(a)). This is a clear signal that flocculation happened, *i.e.,* small Ag agglomerates attracted each other and formed fewer but larger agglomerates. When the standing time was further extended, overlapped backscattering profiles at the middle part of ink samples appeared. This did not mean the inks became more stable after flocculation, but sedimentation started. The overlapped profiles indicated the status at the middle part was relatively constant, which derived from the fact that there was a relative balance between the amount of particles settling into and out of this region. Thus, the backscattering intensity decreasing at the top part and increasing at the bottom part happened at the same time.

The height of middle balance part was shorter with longer standing time and finally disappeared. The onset and period of this middle-stable stage indicate sedimentation speed and ink stability, which was 6-7 min, 10-25 min and 10-20 min for the inks ultrasonicated for 1h, 4h and 7h. After 30 min, significant backscattering intensity decreasing and increasing was detected respectively with 1/4 height as the dividing point for the UB-1h ink, but only a pretty minor variation was observed for the UB-4h ink and UB-7h ink (Fig. S9(a)). Therefore, the UB-1h ink had the fastest flocculation and sedimentation, and the UB-4h ink had the best stability (Fig. 4(a) and Fig. S9(b)). The similar sedimentation behavior of UB-4h ink and UB-7h ink means there is a critical ultrasonication time beyond which the ink stability cannot be further improved, even though the agglomerates can still be broken down a little bit more (Fig. 4(c)). The inks with Nafion were much more stable compared with the extremely fast sedimentation of inks without Nafion. The stability discrepancy of these inks stemmed from different repulsions between agglomerates. The steric hindrance provided by Nafion was the main source of repulsive forces. In addition, due to the absorption of Nafion on the particle surface, the smaller particle size suggested particle fusion was also alleviated by preventing them from getting close (Fig.3, Fig. 4(c), Fig. S7 and S8).

Taken together, the main repulsive force origins from the steric hindrance from Nafion, which played a major role in ink stability improvement. An appropriate extension of ultrasonication can further stabilize the ink by deagglomeration and enhancing the interactions between Nafion and Ag particles.

Regarding the inks prepared by roller mixing, only RM-2h ink appeared obvious flocculation in the first 5 min (Fig. 4(d)). After 30 min, RM-4h ink had the weakest flocculation, whereas RM-2h ink had the most flocculation (Fig. S10). The large average particle size (~1400 nm) of RM-2h ink could be responsible for the most instability. In the other inks, the average particle sizes varied little (between 600-800 nm) (Fig. 4(f)). For both UB-inks and RM-inks, more serious flocculation at longer dispersing time derived from the fact that too much dispersing energy weakened the Ag particles-Nafion network and Nafion adsorption. On the other hand, even though the average particle size increase was not detected by DLS (Fig. 4(c)(f)), we still expected more large-agglomerates in the ink with longer treatment according to the observation in section 3.1. The inconsistency could be due to the fact that large particles were still quite a small minority, which has little effect on the average size. However, the more large-particles produced by either sintering or mechanical rolling could be a reason for less ink stability.

Compared with ultrasonication, the average particle sizes in roller mixed inks were roughly twice or thrice larger owing to mechanical rolling. Even so, roller mixing still provided much more stable ink. The stability

increased about 20 times for the standing time of 5 min and 8 times for 30 min by comparing the instability indexes of UB-7h ink and RM-4h ink. Such a dramatic improvement likely resulted from the promotion of interactions between particles and Nafion. The ionomer absorption and particle-ionomer network could be much more enhanced in roller-mixed inks. Rheology experiments also evidenced it. As shown in Fig.4(g), the viscosity of inks dispersed by roller mixing was about 2 times that dispersed by ultrasonication. Larger particles have been proven to affect viscosity adversely [62], and roller mixing had little improvement on the viscosity of Nafion dispersion (Fig. 4(g)). Therefore, the higher viscosity of RM-ink was ascribed to stronger particle-ionomer interactions. These enhanced interactions may derive from firmer attachment, higher and thicker surface coverage of Nafion on silver particles.

The viscosity evolution of both inks has two stages: shear-thickening at low shear-rates and shear-thinning at high shear rates. At low shear rates, the interparticle forces dominated [63]. The shear flow generated strong local anisotropy and suppressed the dispersion, which gave rise to Ag particle clusters and large stress fluctuations. These further led to high dissipation and thus a high shear viscosity. At high shear rates, the strong shear flow destroyed the Ag particle clusters and caused particle rearrangement, which resulted in organized streamlines and reduced viscosity. Its higher transition shear rate between shear thickening and shear thinning (200 s^{-1} for roller mixing vs. 40 s^{-1} for ultrasonication) also suggested stronger interparticle repulsive forces. It is worth noting that the viscosity of the UB-ink gradually approached that of corresponding Nafion dispersion at a high shear rate. This is clear evidence of weak interactions between Ag particles and Nafion. In contrast, the weaker shear thinning for roller-mixed ink suggested a more robust particle-ionomer network. In summary, roller mixing is a more efficient dispersing technique that brings the catalyst ink higher viscosity, slower sedimentation and better stability by strengthening particle-ionomer interactions. Therefore, all the inks studies below in this section were dispersed by roller mixing.

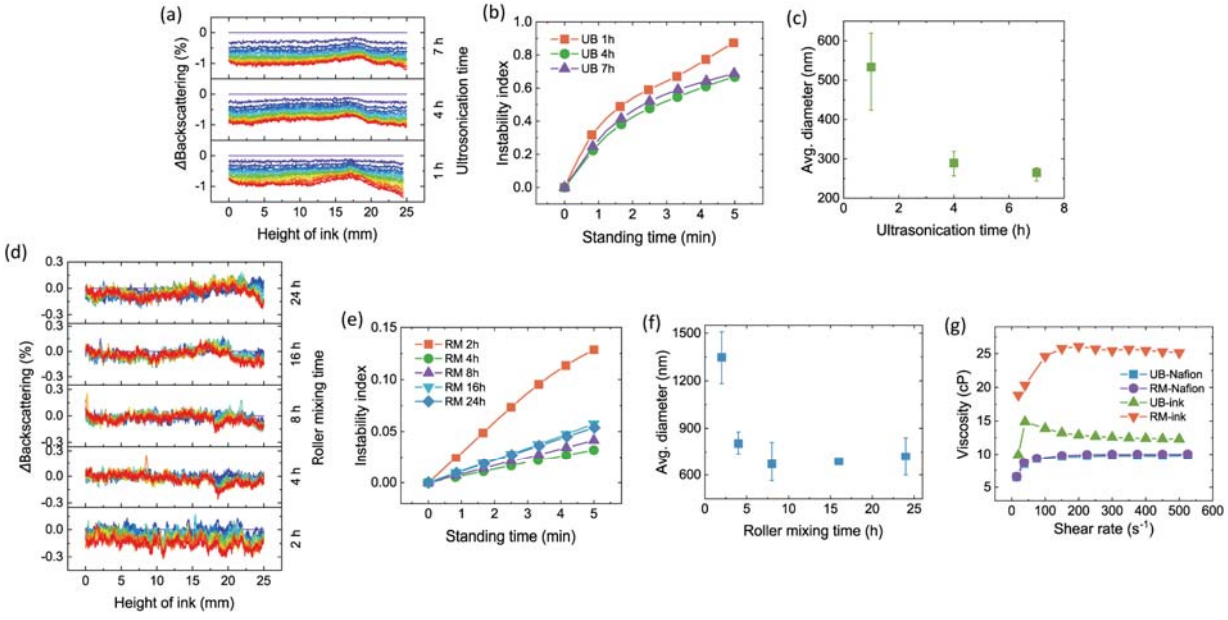

Fig. 4 The sedimentation dynamics spectra, instability index and average particle size evolution with different treating time of ultrasonic bath (a, b, c) and roller mixing (d, e, f). The sedimentation dynamics spectra were colored (violet to red) according to standing time (0 to 5 min). (g) The viscosity of roller-mixed ink (24h), ultrasonicated ink (1h) and corresponding Nafion dispersion. The Nafion dispersion had the same concentration as that in catalyst inks and was ultrasonicated/roller mixed for 30 min.

Nafion content. Steric stabilization is generally achieved by adsorbing or covalently bonding an amphiphilic polymer onto the surface of particles and the chains of polymers stretch into the continuous phase [35, 64]. The sedimentation dynamics spectra and instability indexes showed 10 wt.% and 20 wt.% Nafion in solid has the best ink stability in 5 min (Fig. 5(a)(b)), only a minor backscattering intensity drop was detected at the very top part. 20 wt.% Nafion ink kept flocculating in 30 min, whereas particle concentrating was detected from the bottom to 3/5 of the ink height for 10 wt.% Nafion ink (Fig. S11(a)).

When there was insufficient ionomer, repulsive forces were not strong enough to keep interparticle distance and particle bridging happened. Therefore, 5 wt.% Nafion ink showed fast flocculation and sedimentation. When there was an excess amount of ionomer, the ionomer concentration between adjacent particles was smaller than that of bulk ink because of more non-adsorbed ionomer. The osmotic pressure caused a closer inter-particle distance and larger particle size (Fig. 5(c)). Therefore, there was more serious depletion flocculation in the 30 and 40 wt.% Nafion inks. An extreme case was the ink without Nafion, which showed very fast sedimentation. The critical role of Nafion in stabilizing ink was highlighted here again, regardless of ink formula and dispersing techniques.

ζ-potential showed a three-stage decreasing trend with Nafion content: 0-5%, 5-30% and 30-50% (Fig. 5(d), Fig. S11(c)). In the first stage, the adsorption of Nafion on silver was clearly proven by a dramatic dropping of ζ-potential from -29 mV to -46 mV. Due to the stronger electrostatic and steric repulsion, the average particle size also declined sharply from ~900 nm to ~500 nm (Fig. 5(c)). In the second stage, ζ-potential showed a linear dropping to -70 mV, whereas it kept almost the same when Nafion content increased from 30% to 50%. This indicated that the adsorption of Nafion was saturated at the critical point of 30%. In conclusion, adsorbed Nafion on silver tuned agglomerates size and enhanced ink stability by increasing electrostatic repulsion and steric hindrance.

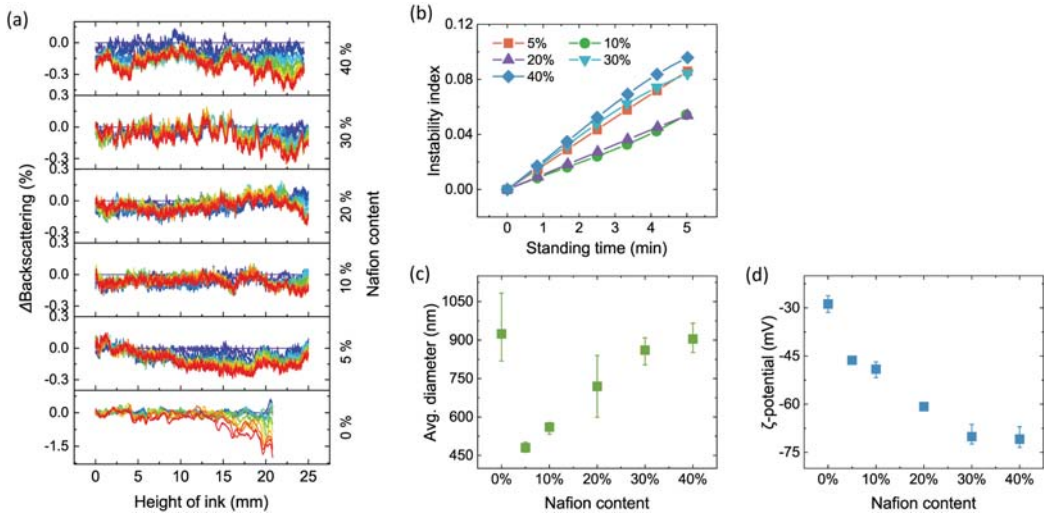

Fig. 5 (a) The sedimentation dynamics spectra, (b) instability index, (c) average particle size and (d) ζ-potential evolution with different Nafion contents in total solid. The sedimentation dynamics spectra were colored (violet to red) according to standing time (0 to 5 min). All the inks were dispersed by roller mixing for 24h.

IPA/water ratio. The effect of dispersing media on ink sedimentation dynamics is shown in Fig. 6(a) and Fig. S12(a). The most apparent feature is IPA-rich catalyst inks showed much slower sedimentation dynamics than water-rich inks. The backscattering profiles overlapped quite well in 5 min for IPA-rich inks, and there was only minor flocculation within 30 min. Another feature was the 30%-IPA and 10%-IPA ink

flocculated quickly in the beginning and entered the sedimentation stage quickly. Both inks had a relatively stable middle balance part, even though there had been supernatant after 30 min. The 50%-IPA ink showed stable flocculation over the 30 min. In Section 3.2, Nafion aggregates were found to be larger and denser in water-rich media but smaller and looser in IPA-rich media. And it was reported that free Nafion aggregates are more numerous in water-rich ink [16, 30, 60]. Therefore, Nafion was likely better dispersed into smaller aggregates and formed a firmer network with Ag particles in IPA-rich inks, which resulted in weaker flocculation and slower sedimentation. The larger and unbonded Nafion aggregates in water-rich conditions resulted in a larger particle size (Fig. 6(c)).

The ζ-potential showed an increase from -77 mV to around -60 mV when the dispersing media transformed from water-rich to IPA-rich (Fig. 6(d)). Apart from the negative effect of alcohol on Ag nanoparticles mentioned in Section 3.1, the evolution of Nafion also plays an important role in the dropping |ζ-potential|. The water-rich environment promotes the sulfuric acid group's dissociation, resulting in a lower electrostatic potential and higher conductivity (Fig. S14). Since both Ag particles and Nafion showed a "saturated" ζ-potential (no obvious change) in IPA rich environment, the complete catalyst ink also had this feature (ζ-potential stopped rising when IPA content reached 2/3). Even though |ζ-potential| in IPA-rich solvents was lower, the sedimentation dynamics were nevertheless slower. Therefore, looser and better dispersed Nafion clusters in IPA-rich solvents are more effective in stabilizing Ag particles than the dense rod-like Nafion aggregates in water-rich solvents.

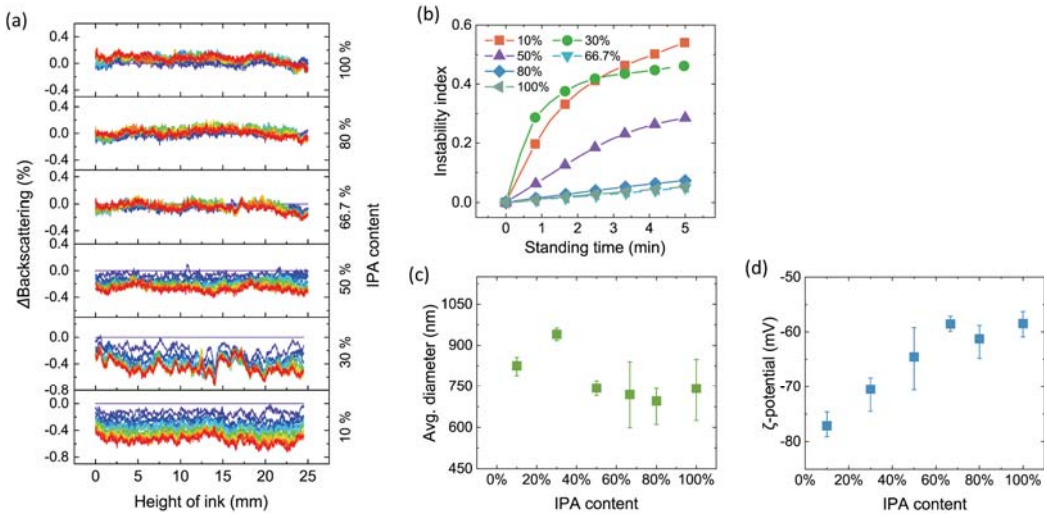

Fig. 6 (a) The sedimentation dynamics spectra, (b) instability index, (c) average particle size and (d) ζ-potential evolution with different IPA/water ratios. The sedimentation dynamics spectra were colored (violet to red) according to standing time (0 to 5 min). All the inks were dispersed by roller mixing for 24h.

Solid content. Solid loading strongly affects catalyst ink stability. At high solid loading, the inter-particle distance is compressed, which results in a more frequent collision and easier agglomeration. Indeed, sedimentation dynamic spectra showed the ink with 40 wt.% solid flocculated the most (Fig. 7(a) and Fig. S13(a)). At the same time, compressed particle motion space caused more adsorption of Nafion on Ag particles. ζ-potential thus dropped from -54 mV to -66 mV (Fig. 7(d)).

Theoretically, less solid content ink has smaller viscosity and is easier to disperse. However, similar to 40%-solid ink, 10%-solid ink also showed more severe flocculation. Especially at the top part, a faster local backscattering intensity drop was detected. And the average particle size in 10%-solid ink was a little larger

than those in 30% and 40%-solid inks (~750 nm vs. ~600 nm, Fig. 7(c)). These indicated that the low solid content ink could be over-dispersed. Since the amount of beads and rolling speed were kept the same for all the inks, the external energy density variation applied on each particle caused by varying solid content was not ignorable. Overdispersion could change particle morphology and create more high-energy active sites on the particle surface, which would further result in the desorption of Nafion, destroying the particle-Nafion network, and re-agglomeration. Therefore, 20%-solid and 30%-solid inks showed the best stability. Especially for the 30%-solid ink, the flocculation was the slowest and the particle size was consistent with that in 40%-solid ink. A balance between solid concentration and dispersing energy was achieved.

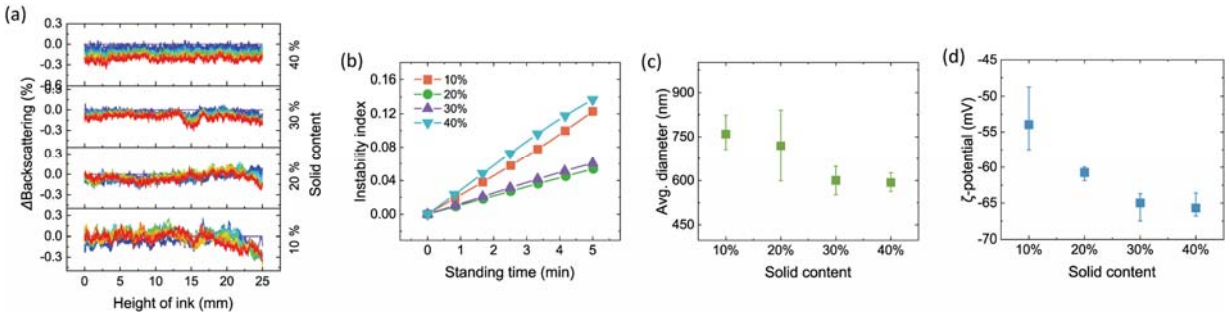

Fig. 7 (a) The sedimentation dynamics spectra, (b) instability index, (c) average particle size and (d) ζ-potential evolution with different solid contents. The sedimentation dynamics spectra were colored (violet to red) according to standing time (0 to 5 min). All the inks were dispersed by roller mixing for 24h.

3.4 Correlating ink stability with coating homogeneity and CO_2R performance

To make clear the influence of catalyst ink stability on the structure formation of CL, coating homogeneity and electrochemical performance, two different inks, the most unstable ink and most stable ink, were picked out. These inks coincidentally belong to the ink groups dispersed by ultrasonication and roller mixing. They showed colossal stability difference in both 5 min and 30 min (Fig. 8(a) and Fig. S15).

Catalyst layers were fabricated by coating the inks directly on GDLs with a doctor blade. After the GDEs were prepared, each of them was cut into 9 pieces equally with a home-designed cutting die to check the coating homogeneity of the catalyst with TGA. As shown in the heating maps (Fig. 8(b)), the loading homogeneity of CL coated by ultrasonicated ink (UB-CL) was much worse than that coated by roller-mixed ink (RM-CL). The average catalyst loading (average ± standard deviation) for UB-1h CL from top to bottom were 2.36±0.32 mg/cm^2, 1.82±0.07 mg/cm^2, 1.51±0.01 mg/cm^2, which showed a clear gradient along the coating direction. At the same time, the loading difference perpendicular to the coating direction was also significant for the top and middle rows, which reached 0.8 and 0.2 mg/cm^2. But the bottom row was relatively homogeneous. The highest loading difference stupendously reached 1.25 mg/cm^2 among the 9 pieces. The loading gradients directly resulted from the fast sedimentation of ultrasonicated inks. As shown in Fig. S16, more big agglomerates settled at the beginning of coating. Thanks to the more stable ink, the average catalyst loadings for RM-4h CL from top to bottom were 2±0.07 mg/cm^2, 2.09±0.02 mg/cm^2, 2.08±0.03 mg/cm^2. The gradients along and perpendicular to the coating direction disappeared, and the homogeneity improved dramatically. Compared with UB-1h CL, the surface of RM-4h CL was much finer and smoother. The cracks on the surface caused by agglomerates were much more mitigated. However, the RM-4h CL appears to have more large-pores than UB-1h CL at cross-section (Fig. 9(c)(f)). This

may be caused by Ag flakes, which were observed both on the surface and inside of RM-4h CL. The Ag flakes with different dimensions were produced by the mechanical rolling of beads during the dispersing process (Fig. S21).

Following the catalyst loading and morphological investigations, the CO_2 reduction performance was tested with a flow cell (Fig. S3). The polarization curves for CO_2RR are shown in Fig. 10(a). The RM-4h GDE had lower cathodic potentials than UB-1h GDE, which is consistent with ink stability and coating homogeneity. At an industry-meaningful current density of 200 mA/cm^2, the cathode potential of RM 4h-GDE was -0.88 V vs. RHE, which is 0.14 V lower than that of UB 1h-GDE. At the same time, the average Faradaic efficiency of CO in 1 h (FE_{CO}) was promoted from 80.5% to 94%, and the Faradaic efficiency of H_2 (FE_{H2}) dropped from 14% to 1.6%. At 300 mA/cm^2, FE_{CO} was dramatically boosted from 38% to 81% and FE_{H2} decreased from 56.5% to 8.7% (Fig. 10(b)). The GDE durability tests were performed at 100 mA/cm^2. The FE_{CO} of UB-1h GDE can only be maintained above 80% for 2 h. In contrast, the FE_{CO} of RM-4h GDE can be held above 80% for more than 12 h (Fig. 10(c)). Less flooding was observed for the RM-4h GDE, which was the main reason for the higher CO Faradaic efficiency. The severe heterogeneity (Fig. S16, S17) of UB-CL led to the inhomogeneous distribution of electrochemically active sites and reaction rates. It further caused uneven consumption of reactants and uneven distribution of heat, electrons and intermediate products. The CL suffered great stress concentration, which could destroy the microstructure of CL and the multiphase boundary. These resulted in the worse performance of UB-1h GDE. The SEM images showed that UB-1h GDE had more and larger cracks after electrolysis at 200 mA/cm^2 for 1 h (Fig. S18). In addition, due to the weak particle/Nafion network in UB ink, more free ionomer aggregates are expected, which was reported to cause depletion flocculation in catalyst ink and reduce the durability of the catalyst layer [65]. Therefore, the dramatically enhanced RM-ink stability suggested improved particle-ionomer interactions (*vide ante*). It ensured not only more uniform CL, but also better durability.

It is worth noting that both RM-24h GDE and UB-7h GDE exhibited lower Faradaic efficiencies of CO (90% and 77% respectively) compared to their counterparts with the same dispersing techniques but shorter dispersing time (*i.e.* RM-4h GDE and UB-1h GDE, Fig. S19). This clearly indicated that more large-aggregates induced by more dispersing energy (sintering and mechanical rolling) led to worse selectivity of CO. However, the cathodic potential of RM-24h GDE was higher than that of RM-4h GDE, whereas the cathodic potential of UB-7h GDE was lower than that of UB-1h GDE. Also, RM-24h ink and UB-1h ink had worse stability. It implied that an improved catalyst-ionomer network contributed to reducing the overpotential of CO_2RR.

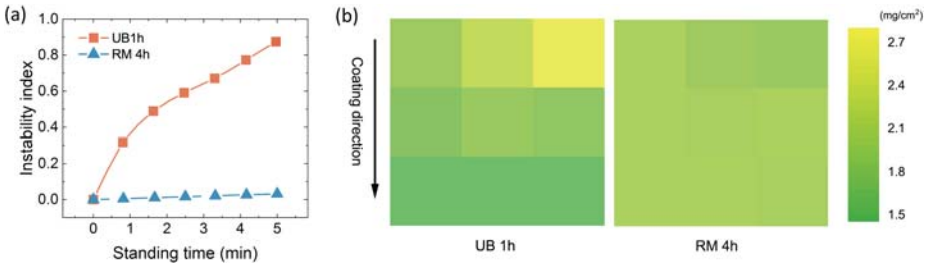

Fig. 8 (a) Comparison of instability index of the best and worst inks. (b) Catalyst loading distribution of catalyst layers fabricated by UB-1h ink and RM-4h ink.

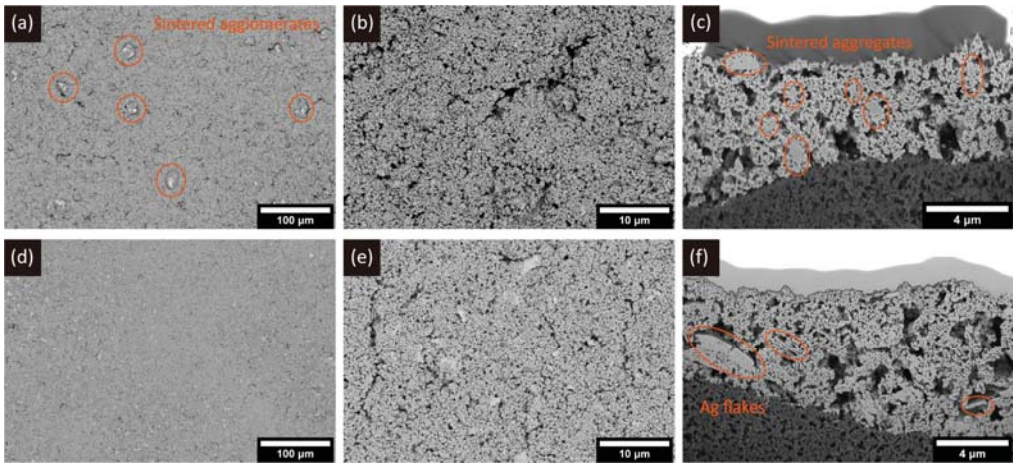

Fig. 9 Surface and cross-section morphology of the catalyst layers fabricated by the UB-1h ink (a-c) and RM-4h ink (d-f).

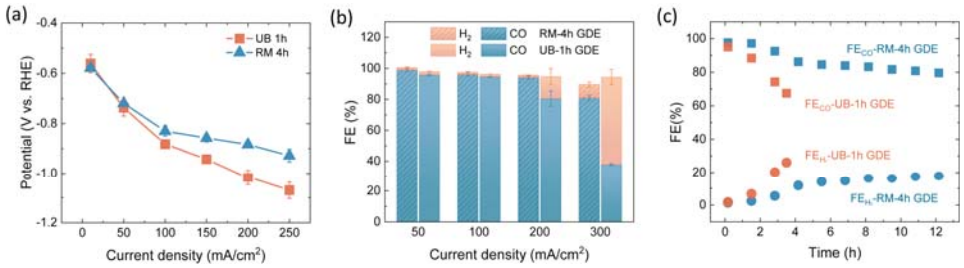

Fig. 10 (a) Polarization curves, (b) Faradic efficiency of CO and H_2 and (c) durability tests at 100 mA/cm^2 of GDEs fabricated by the most stable and most unstable inks (UB-1h ink and RM-4h ink).

3.5 Discussion

The interactions of Ag particles/Nafion, Ag particles/solvents, Nafion/solvents determine the ink sedimentation dynamics, multiscale structure of the catalyst layer and further the performance of CO_2 reduction. The evolution of Ag catalyst ink can be divided into three stages: stable, flocculation and sedimentation (Fig. 11). At the stable stage, the catalyst ink retains the status the moment exactly after dispersing. Then attraction and combination of catalyst particles happen, forming larger agglomerates. When the agglomerates grow beyond the critical size, the repulsive forces between particles cannot withstand gravity, and sedimentation starts. More and more particles settle downside slowly from the top part, the backscattering at the top part becomes less and less and at the bottom part higher and higher until supernate appears. A well-dispersed catalyst ink should keep at the stable stage for as long as possible. We must point out that there is no absolute stable stage due to the ubiquitous Brownian movement and flocculation. We expect the detected SMLS signal difference to be as small as possible for a given time (characteristic time). The applicability of a specific ink depends on the coating techniques to be used. The characteristic time is much longer than the actual coating time. According to our experience, the SMLS signal difference is supposed to be within 0.1% in the characteristic time of 10 min and 24 h for doctor blading and ultrasonic spray coating, respectively.

The sedimentation dynamics are mainly determined by the repulsive force between particles provided by the ionomer. Derjaguin-Landau-Verway-Overbeak (DLVO) theory, describing and predicting particle behaviors in dispersion by considering Van der Waals force and electrostatic repulsive force between

particles, is not applicable for extremely complex catalyst inks. In the best case, extended DLVO theory (Osmotic repulsion, steric repulsion, etc. are included) can provide some perspectives and qualitative information on aggregation and sedimentation behaviors analysis [66]. However, measuring the indicators or characteristic parameters of these complex repulsions in catalyst ink is difficult. Actually, ζ-potential is the only measurable and the most used parameter to indicate ink stability based on (extended) DLVO theory [61]. Our results clearly indicated the decoupling of ζ-potential and ink stability (Fig. 5-7). ζ-potential is a good indicator of electrostatic repulsion, but not of ink stability. The effectiveness of ζ-potential for predicting dispersion stability depends on the contribution of electrostatic repulsion to the total repulsion. Our results suggest electrostatic repulsion contributed quite little in a complex and polydisperse catalyst ink system. Similarly, particle size, one of the many factors affecting ink stability, is also not necessarily determinative. Optimizing only the ζ-potential and particle size may not make much sense, since it is impossible not to cause changes in other factors. Therefore, SMLS is the most direct and effective way to acquire the actual ink dynamics/stability information in detail and provide validation for related mathematical models and simulations.

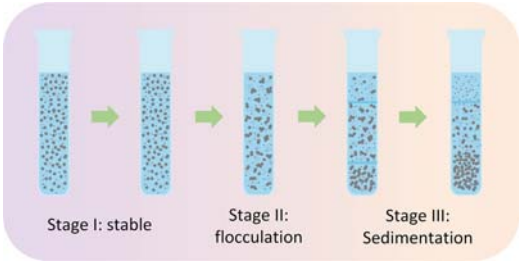

Fig. 11 Illustration of catalyst ink evolution.

As the main source of repulsive forces, steric hindrance derived from ionomer depends on the particle-ionomer network, including the adsorption of ionomer on catalyst particles, structure and morphology of ionomer aggregates. The adsorption of Nafion depends on the intrinsic properties of catalyst materials (such as surface morphology, capping agent, synthesis methodology, agglomeration status in powder, etc.). For Pt/C catalyst ink, the adsorption of Nafion with Pt/C was reported to take place through the bonding of backbones on carbon, and sulfuric acid group and -CF_3 group on side chains bonding with platinum [67–69]. However, our results suggested the adsorption of Nafion on Ag particles is quite weak, which resulted in much lower ink viscosity and stability than Pt/C ink. The key point to improve ink stability is enhancing Nafion adsorption on catalyst particles and the following catalyst particles-Nafion network.

Solvent is another crucial factor affecting ink status by modulating ionomer morphology, structure and adsorption. The complex morphologies and structures of Nafion in different solvents are not determined by a single parameter of solvents, such as the dielectric constant as generally believed, but by the balance of various parameters acting together (like interfacial energy, dielectric constant, solubility and elastic energy of backbone and side chains, etc.). As is shown in Fig. 12, the looser, smaller and better dispersed Nafion aggregates in an IPA-rich environment form a firmer network with Ag particles, but the rod-like aggregates in a water-rich environment cannot produce enough interactions to stabilize the ink. And at higher Nafion content, too much free ionomer causes larger agglomerates and accelerates flocculation due to osmotic pressure.

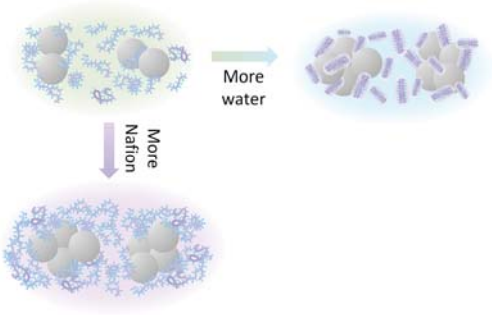

Fig. 12 Illustration of catalyst particles-Nafion interactions under the effect of solvents and Nafion content.

Agglomeration in catalyst ink is crucial to sedimentation dynamics and CO_2R performance. Our results showed ultrasonic bath is not effective enough to establish strong catalyst particle-ionomer. The particle sintering caused by ultrasonication was reported for the first time. Small sintered-aggregates are distributed everywhere in the cross-section image of UB-CL (Fig. 9(c)). The cross-section of large sintered-aggregates (ca. 20 μm) showed a structure similar to raisin bread, which features a smooth surface wrapping a porous structure with scattered solid aggregates (Fig. S20). The dense sintered outer layer blocks the diffusion of CO_2 and products, and the Ag particles wrapped inside cannot effectively perform CO_2RR. The sintered aggregates reduced the electrochemical active sites in the catalyst layers significantly. In addition, the sintered agglomerates could produce pinholes on the membrane of zero-gap cells, resulting in cell failure. Ultrasonication is widely used in ink preparation for fuel cells, particles fusion is rarely reported [8]. In this work, the high particle content results in an increased particle collision frequency, and the melting point is comparatively low. Therefore, silver showed much less robustness to ultrasonication than platinum. On one hand, extending ultrasonication time caused particle fusion and less active sites for CO_2R. On the other hand, too little ultrasonication is not enough to produce strong interactions between Ag particles and Nafion. Striking a balance between *Scylla* and *Charybdis* is always tricky. By comparison, roller mixing is a more practical approach to establishing the particle/Nafion network than ultrasonication. Even though Ag flakes produced by mechanical rolling are detrimental to ink stability and CO_2R performance, our results showed their negative effect was not as serious as those agglomerates introduced by ultrasonication.

The CO_2R performance in a near-neutral environment using commercial catalyst nanoparticles is usually taken as a negative reference to highlight the better performance of new catalyst materials, new GDE structures or different operation conditions [70–72]. Table S1 summarizes the performance of CO_2R to CO using commercial Ag NPs published in recent years. The previous works did not pay enough attention to ink preparation and CL fabrication, which underestimated the performance of commercial Ag catalysts. In this work, the highest reported CO selectivity of 94% at an industrial meaningful current density of 200 mA/cm^2 was achieved by rational design of ink formulation, dispersing and fabrication processes. This performance is better than most new materials or structures in a near-neutral environment [70–73]. Based on the understanding of each ink ingredient's role and correlations of a series of preparation steps, a scalable manufacturing methodology of robust Ag GDEs to achieve optimal CO_2R performance was developed and validated. Due to the good universality of the devices used, this methodology, from catalyst ink preparation and stability evaluation to CL fabrication, is applicable to different catalysts (metal, metal oxide, etc.) for different reactions such as ORR, OER or HER in fuel cell and water electrolysis applications. It will not only provide a meaningful reference for lab applications (fast and reproducible GDE fabrication aiming at new catalysts, ionomers, membranes or operation conditions development), but also provide a

steppingstone to industrial applications (GDE fabrication aiming at large scale, good durability and quality of conformance).

4. Conclusion

The roles of Ag particles, Nafion, solvents and their interactions in catalyst ink were systematically studied from simple binary inks to complete inks. Our results showed Ag agglomerates can be broken down more efficiently in water than in alcohols due to stronger inter-particle repulsive forces induced by water disassociation. However, applicable catalyst ink can only be obtained by introducing ionomer. Subsequently, the catalyst ink status was systemically characterized and evaluated by static multiple light scattering. The three stages of catalyst ink evolution, *i.e.,* stable, flocculation and sedimentation, were identified. Slower ink sedimentation dynamics were demonstrated in IPA-rich solvents, which was ascribed to the better dispersed Nafion aggregates and further enhanced Ag particle-Nafion network. Inks with Nafion and solid content of 10-20 wt.% and 20-30 wt.% respectively were found to have the optimum stability. Finally, the correlations between multi-component interactions, ink stability, coating homogeneity and CO_2R performance were revealed. Strong Ag particle-Nafion interactions established by roller mixing extended the ink stable stage and improved catalyst layer homogeneity dramatically, which boosted CO selectivity from 80.5% to 94% and from 38% to 81% at an industrial meaningful current density of 200 and 300 mA/cm^2, respectively. The durability of GDE was also improved for 6 times at 100 mA/cm^2. However, such interactions cannot be established effectively by ultrasonication. The catalyst loading gradient and catalyst particle sintering resulting from ultrasound caused more severe flooding and worse CO selectivity. At the same time, a scalable manufacturing methodology of robust Ag GDEs, from ink preparation to CL fabrication, was developed and validated.

Author contributions

G. Liu conceived and designed all the experiments. D. Mclaughlin conducted SEM characterization on GDEs. G. Liu and D. McLauhlin designed the CO_2R testing system. S. Thiele and C. Pham conceived and supervised the project. All authors discussed the results and contributed to the manuscript preparation.

Conflicts of interest

There are no conflicts to declare.

Acknowledgements

This work was supported by Federal Ministry of Education and Research, Germany (BMBF) under the project No. 033RC028. The authors appreciate the meaningful discussion with Markus Bierling, Marc Ayoub and Maximillian Wagner, and the help of Dominik Seeberger, Anna Freiberg, Dominik Kraus, Thomas Böhm, Britta Mayerhöfer and Manuel Hegelheimer with the experimental devices.

References

1. IEA CO2 Emissions from Fuel Combustion, 2019th edn. International Energy Agency, Paris
2. Pachauri RK, Mayer L (eds) (2015) The Fifth Assessment Report of the Intergovernmental Panel on Climate Change: Climate Change 2014: Synthesis Report. Intergovernmental Panel on Climate Change, Geneva, Switzerland
3. Jordaan SM, Wang C (2021) Electrocatalytic conversion of carbon dioxide for the Paris goals. Nat Catal 4:915–920. https://doi.org/10.1038/s41929-021-00704-z
4. Wilbur S, Williams M, Williams R et al. (eds) (2012) Toxicological Profile for Carbon Monoxide. Agency for Toxic Substances and Disease Registry (US)
5. Nitopi S, Bertheussen E, Scott SB et al. (2019) Progress and Perspectives of Electrochemical CO2 Reduction on Copper in Aqueous Electrolyte. Chem Rev 119:7610–7672. https://doi.org/10.1021/acs.chemrev.8b00705
6. Weng L-C, Bell AT, Weber AZ (2018) Modeling gas-diffusion electrodes for CO2 reduction. Phys Chem Chem Phys 20:16973–16984. https://doi.org/10.1039/c8cp01319e
7. Nguyen TN, Dinh C-T (2020) Gas diffusion electrode design for electrochemical carbon dioxide reduction. Chem Soc Rev 49:7488–7504. https://doi.org/10.1039/d0cs00230e
8. Pollet BG, Kocha SS (2022) Using Ultrasound to Effectively Homogenise Catalyst Inks: Is this Approach Still Acceptable? : Recommendations on the use of ultrasound for mixing catalyst inks. Johnson Matthey Technology Review 66:61–76. https://doi.org/10.1595/205651321X16196162869695
9. Wang M, Park JH, Kabir S et al. (2019) Impact of Catalyst Ink Dispersing Methodology on Fuel Cell Performance Using in-Situ X-ray Scattering. ACS Appl Energy Mater 2:6417–6427. https://doi.org/10.1021/acsaem.9b01037
10. Lees EW, Mowbray BAW, Salvatore DA et al. (2020) Linking gas diffusion electrode composition to CO 2 reduction in a flow cell. J. Mater. Chem. A 8:19493–19501. https://doi.org/10.1039/D0TA03570J
11. Liu H, Ney L, Zamel N et al. (2022) Effect of Catalyst Ink and Formation Process on the Multiscale Structure of Catalyst Layers in PEM Fuel Cells. Applied Sciences 12:3776. https://doi.org/10.3390/app12083776
12. Hatzell KB, Dixit MB, Berlinger SA et al. (2017) Understanding inks for porous-electrode formation. J. Mater. Chem. A 5:20527–20533. https://doi.org/10.1039/C7TA07255D
13. Sousa L de, Harmoko C, Benes N et al. (2021) Optimizing the Ink Formulation for Preparation of Cu-Based Gas Diffusion Electrodes Yielding Ethylene in Electroreduction of CO 2. ACS EST Eng 1:1649–1658. https://doi.org/10.1021/acsestengg.1c00228
14. Martić N, Reller C, Macauley C et al. (2019) Paramelaconite‐Enriched Copper‐Based Material as an Efficient and Robust Catalyst for Electrochemical Carbon Dioxide Reduction. Advanced Energy Materials 9:1901228. https://doi.org/10.1002/aenm.201901228
15. Ren H, Meng X, Lin Y et al. (2022) Microstructure formation mechanism of catalyst layer and its effect on fuel cell performance: Effect of dispersion medium composition. Journal of Energy Chemistry 73:588–598. https://doi.org/10.1016/j.jechem.2022.06.034
16. Takahashi S, Mashio T, Horibe N et al. (2015) Analysis of the Microstructure Formation Process and Its Influence on the Performance of Polymer Electrolyte Fuel-Cell Catalyst Layers. ChemElectroChem 2:1560–1567. https://doi.org/10.1002/celc.201500131

17. Kusano T, Hiroi T, Amemiya K et al. (2015) Structural evolution of a catalyst ink for fuel cells during the drying process investigated by CV-SANS. Polym J 47:546–555. https://doi.org/10.1038/pj.2015.36
18. Park H-S, Cho Y-H, Cho Y-H et al. (2007) Performance enhancement of PEMFC through temperature control in catalyst layer fabrication. Electrochimica Acta 53:763–767. https://doi.org/10.1016/j.electacta.2007.07.046
19. Scheepers F, Stähler A, Stähler M et al. (2019) Steering and in situ monitoring of drying phenomena during film fabrication. J Coat Technol Res 16:1213–1221. https://doi.org/10.1007/s11998-019-00206-5
20. Kameyama K, Komoda Y, Suzuki H et al. (2007) Optimization of Preparation and Drying Conditions of Titanium Dioxide Slurry for Coating on a Plastic Substrate. J Chem Eng Japan / JCEJ 40:973–979. https://doi.org/10.1252/jcej.07WE026
21. Dixit MB, Harkey BA, Shen F et al. (2018) Catalyst Layer Ink Interactions That Affect Coatability. J Electrochem Soc 165:F264-F271. https://doi.org/10.1149/2.0191805jes
22. Gong Q, Li C, Liu Y et al. (2021) Effects of Ink Formulation on Construction of Catalyst Layers for High-Performance Polymer Electrolyte Membrane Fuel Cells. ACS Appl Mater Interfaces 13:37004–37013. https://doi.org/10.1021/acsami.1c06711
23. Kumano N, Kudo K, Suda A et al. (2019) Controlling cracking formation in fuel cell catalyst layers. Journal of Power Sources 419:219–228. https://doi.org/10.1016/j.jpowsour.2019.02.058
24. Xu F, Zhang H, Ilavsky J et al. (2010) Investigation of a catalyst ink dispersion using both ultra-small-angle X-ray scattering and cryogenic TEM. Langmuir 26:19199–19208. https://doi.org/10.1021/la1028228
25. Khandavalli S, Park JH, Kariuki NN et al. (2019) Investigation of the Microstructure and Rheology of Iridium Oxide Catalyst Inks for Low-Temperature Polymer Electrolyte Membrane Water Electrolyzers. ACS Appl Mater Interfaces 11:45068–45079. https://doi.org/10.1021/acsami.9b14415
26. Yang F, Le Xin, Uzunoglu A et al. (2017) Investigation of the Interaction between Nafion Ionomer and Surface Functionalized Carbon Black Using Both Ultrasmall Angle X-ray Scattering and Cryo-TEM. ACS Appl Mater Interfaces 9:6530–6538. https://doi.org/10.1021/acsami.6b12949
27. Yang D, Guo Y, Tang H et al. (2021) Influence of the dispersion state of ionomer on the dispersion of catalyst ink and the construction of catalyst layer. International Journal of Hydrogen Energy 46:33300–33313. https://doi.org/10.1016/j.ijhydene.2021.07.172
28. Khandavalli S, Iyer R, Park JH et al. (2020) Effect of Dispersion Medium Composition and Ionomer Concentration on the Microstructure and Rheology of Fe-N-C Platinum Group Metal-free Catalyst Inks for Polymer Electrolyte Membrane Fuel Cells. Langmuir 36:12247–12260. https://doi.org/10.1021/acs.langmuir.0c02015
29. Shukla S, Bhattacharjee S, Weber AZ et al. (2017) Experimental and Theoretical Analysis of Ink Dispersion Stability for Polymer Electrolyte Fuel Cell Applications. J Electrochem Soc 164:F600-F609. https://doi.org/10.1149/2.0961706jes
30. Kumano N, Kudo K, Akimoto Y et al. (2020) Influence of ionomer adsorption on agglomerate structures in high-solid catalyst inks. Carbon 169:429–439. https://doi.org/10.1016/j.carbon.2020.07.047
31. Takamuku T, Saisho K, Nozawa S et al. (2005) X-ray diffraction studies on methanol–water, ethanol–water, and 2-propanol–water mixtures at low temperatures. Journal of Molecular Liquids 119:133–146. https://doi.org/10.1016/j.molliq.2004.10.020

32. Li F, Men Z, Li S et al. (2018) Study of hydrogen bonding in ethanol-water binary solutions by Raman spectroscopy. Spectrochim Acta A Mol Biomol Spectrosc 189:621–624. https://doi.org/10.1016/j.saa.2017.08.077
33. Egashira K, Nishi N (1998) Low-Frequency Raman Spectroscopy of Ethanol−Water Binary Solution: Evidence for Self-Association of Solute and Solvent Molecules. J Phys Chem B 102:4054–4057. https://doi.org/10.1021/jp9806359
34. Zhang H, Gilbert B, Huang F et al. (2003) Water-driven structure transformation in nanoparticles at room temperature. Nature 424:1025–1029. https://doi.org/10.1038/nature01845
35. Shrestha S, Wang B, Dutta P (2020) Nanoparticle processing: Understanding and controlling aggregation. Adv Colloid Interface Sci 279:102162. https://doi.org/10.1016/j.cis.2020.102162
36. Kosmulski M, Matijevic E (1992) ζ-potentials of silica in water-alcohol mixtures. Langmuir 8:1060–1064. https://doi.org/10.1021/la00040a008
37. Doktycz SJ, Suslick KS (1990) Interparticle collisions driven by ultrasound. Science 247:1067–1069. https://doi.org/10.1126/science.2309118
38. Prozorov T, Prozorov R, Suslick KS (2004) High velocity interparticle collisions driven by ultrasound. J Am Chem Soc 126:13890–13891. https://doi.org/10.1021/ja049493o
39. Pollet BG (2010) The use of ultrasound for the fabrication of fuel cell materials. International Journal of Hydrogen Energy 35:11986–12004. https://doi.org/10.1016/j.ijhydene.2010.08.021
40. Yeung SA, Hobson R, Biggs S et al. (1993) Formation of gold sols using ultrasound. J Chem Soc., Chem Commun 0:378. https://doi.org/10.1039/C39930000378
41. Fouad WA, Le Wang, Haghmoradi A et al. (2016) Understanding the Thermodynamics of Hydrogen Bonding in Alcohol-Containing Mixtures: Cross-Association. J Phys Chem B 120:3388–3402. https://doi.org/10.1021/acs.jpcb.5b12375
42. Díaz-Torres R, Alvarez S (2011) Coordinating ability of anions and solvents towards transition metals and lanthanides. Dalton Trans 40:10742–10750. https://doi.org/10.1039/C1DT11000D
43. Burrows ND, Kesselman E, Sabyrov K et al. (2014) Crystalline nanoparticle aggregation in non-aqueous solvents. CrystEngComm 16:1472–1481. https://doi.org/10.1039/C3CE41584H
44. Kirly Z, Turi L, Dkny I et al. (1996) Van der Waals attraction between Stber silica particles in a binary solvent system. Colloid Polym Sci 274:779–787. https://doi.org/10.1007/BF00654674
45. Podgornik R, Cevc G, Žekš B (1987) Solvent structure effects in the macroscopic theory of van der Waals forces. J Chem Phys 87:5957–5967. https://doi.org/10.1063/1.453519
46. Deegan RD, Bakajin O, Dupont TF et al. (1997) Capillary flow as the cause of ring stains from dried liquid drops. Nature 389:827–829. https://doi.org/10.1038/39827
47. Monteiro MCO, Philips MF, Schouten KJP et al. (2021) Efficiency and selectivity of CO2 reduction to CO on gold gas diffusion electrodes in acidic media. Nat Commun 12:4943. https://doi.org/10.1038/s41467-021-24936-6
48. Jeanty P, Scherer C, Magori E et al. (2018) Upscaling and continuous operation of electrochemical CO 2 to CO conversion in aqueous solutions on silver gas diffusion electrodes. Journal of CO2 Utilization 24:454–462. https://doi.org/10.1016/j.jcou.2018.01.011
49. Kusoglu A, Weber AZ (2017) New Insights into Perfluorinated Sulfonic-Acid Ionomers. Chem Rev 117:987–1104. https://doi.org/10.1021/acs.chemrev.6b00159
50. Pierre Aldebert, Bernard Dreyfus, Michel Pineri (1986) Small-angle neutron scattering of perfluorosulfonated ionomers in solution. Macromolecules 19:2651–2653. https://doi.org/10.1021/ma00164a035

51. Aldebert P, Dreyfus B, Gebel G et al. (1988) Rod like micellar structures in perfluorinated ionomer solutions. J Phys France 49:2101–2109. https://doi.org/10.1051/jphys:0198800490120210100
52. Gebel G, Loppinet B (1996) Colloidal structure of ionomer solutions in polar solvents. Journal of Molecular Structure 383:43–49. https://doi.org/10.1016/S0022-2860(96)09266-6
53. Loppinet B, Gebel G (1998) Rodlike Colloidal Structure of Short Pendant Chain Perfluorinated Ionomer Solutions. Langmuir 14:1977–1983. https://doi.org/10.1021/la9710987
54. Loppinet B, Gebel G, Williams CE (1997) Small-Angle Scattering Study of Perfluorosulfonated Ionomer Solutions. J Phys Chem B 101:1884–1892. https://doi.org/10.1021/jp9623047
55. Tarokh A, Karan K, Ponnurangam S (2020) Atomistic MD Study of Nafion Dispersions: Role of Solvent and Counterion in the Aggregate Structure, Ionic Clustering, and Acid Dissociation. Macromolecules 53:288–301. https://doi.org/10.1021/acs.macromol.9b01663
56. Ghelichi M, Malek K, Eikerling MH (2016) Ionomer Self-Assembly in Dilute Solution Studied by Coarse-Grained Molecular Dynamics. Macromolecules 49:1479–1489. https://doi.org/10.1021/acs.macromol.5b02158
57. Welch C, Labouriau A, Hjelm R et al. (2012) Nafion in Dilute Solvent Systems: Dispersion or Solution? ACS Macro Lett 1:1403–1407. https://doi.org/10.1021/mz3005204
58. Li S, Terao K, Sato T (2018) Colloidal Dispersion of a Perfluorosulfonated Ionomer in Water–Methanol Mixtures. Polymers 10:72. https://doi.org/10.3390/polym10010072
59. Yamaguchi M, Matsunaga T, Amemiya K et al. (2014) Dispersion of Rod-like Particles of Nafion in Salt-Free Water/1-Propanol and Water/Ethanol Solutions. J Phys Chem B 118:14922–14928. https://doi.org/10.1021/jp506814m
60. Ngo TT, Yu TL, Lin H-L (2013) Influence of the composition of isopropyl alcohol/water mixture solvents in catalyst ink solutions on proton exchange membrane fuel cell performance. Journal of Power Sources 225:293–303. https://doi.org/10.1016/j.jpowsour.2012.10.055
61. Berlinger SA, McCloskey BD, Weber AZ (2018) Inherent Acidity of Perfluorosulfonic Acid Ionomer Dispersions and Implications for Ink Aggregation. J Phys Chem B 122:7790–7796. https://doi.org/10.1021/acs.jpcb.8b06493
62. Jia-Fei Z, Zhong-Yang L, Ming-Jiang N et al. (2009) Dependence of Nanofluid Viscosity on Particle Size and pH Value. Chinese Phys Lett 26:66202. https://doi.org/10.1088/0256-307X/26/6/066202
63. Wagner NJ, Brady JF (2009) Shear thickening in colloidal dispersions. Physics Today 62:27–32
64. Wang Q, Fu S, Yu T (1994) Emulsion polymerization. Progress in Polymer Science 19:703–753. https://doi.org/10.1016/0079-6700(94)90031-0
65. Woo S, Lee S, Taning AZ et al. (2020) Current understanding of catalyst/ionomer interfacial structure and phenomena affecting the oxygen reduction reaction in cathode catalyst layers of proton exchange membrane fuel cells. Current Opinion in Electrochemistry 21:289–296. https://doi.org/10.1016/j.coelec.2020.03.006
66. Hotze EM, Phenrat T, Lowry GV (2010) Nanoparticle aggregation: challenges to understanding transport and reactivity in the environment. Journal of Environmental Quality 39:1909–1924. https://doi.org/10.2134/jeq2009.0462
67. Mashio T, Ohma A, Tokumasu T (2016) Molecular Dynamics Study of Ionomer Adsorption at a Carbon Surface in Catalyst Ink. Electrochimica Acta 202:14–23. https://doi.org/10.1016/j.electacta.2016.04.004
68. Kendrick I, Kumari D, Yakaboski A et al. (2010) Elucidating the ionomer-electrified metal interface. J Am Chem Soc 132:17611–17616. https://doi.org/10.1021/ja1081487

69. Zeng J, Jean D, Ji C et al. (2012) In situ surface-enhanced Raman spectroscopic studies of nafion adsorption on Au and Pt electrodes. Langmuir 28:957–964. https://doi.org/10.1021/la2035455
70. Dinh C-T, García de Arquer FP, Sinton D et al. (2018) High Rate, Selective, and Stable Electroreduction of CO 2 to CO in Basic and Neutral Media. ACS Energy Lett 3:2835–2840. https://doi.org/10.1021/acsenergylett.8b01734
71. Wu X, Guo Y, Sun Z et al. (2021) Fast operando spectroscopy tracking in situ generation of rich defects in silver nanocrystals for highly selective electrochemical CO2 reduction. Nat Commun 12:660. https://doi.org/10.1038/s41467-021-20960-8
72. Gabardo CM, Seifitokaldani A, Edwards JP et al. (2018) Combined high alkalinity and pressurization enable efficient CO 2 electroreduction to CO. Energy Environ Sci 11:2531–2539. https://doi.org/10.1039/C8EE01684D
73. Verma S, Lu X, Ma S et al. (2016) The effect of electrolyte composition on the electroreduction of CO2 to CO on Ag based gas diffusion electrodes. Phys Chem Chem Phys 18:7075–7084. https://doi.org/10.1039/c5cp05665a